IMA Journal of Applied Mathematics (2011) **76**, 146–168
doi:10.1093/imamat/hxq061
Advance Access publication on December 23, 2010

Interactive buckling in sandwich beam-columns

STYLIANOS YIATROS*,† AND M. AHMER WADEE
Department of Civil and Environmental Engineering, Imperial College of Science, Technology and Medicine, London SW7 2AZ, UK
*Corresponding author: stylianos.yiatros@brunel.ac.uk

[Received on 17 November 2009; revised on 8 June 2010; accepted on 16 November 2010]

Recent work on localized buckling with different core bending theories in sandwich struts is adapted for a sandwich beam-column that combines the effects of bending and compression. The two distinct bifurcations present in the pure compression case are replaced by a single pitchfork bifurcation point that combines local and global buckling behaviour. Several models with a various number of degrees of freedom (DOFs) are developed to account for the explicit effect of end moments. All models are formulated using total potential energy and variational principles, which are used to derive the governing equations that are solved using the numerical continuation package AUTO97. Results are validated with a finite element model formulated in the commercial package ABAQUS. Comparisons with the interactive buckling profiles and the mechanical response in the nonlinear range are very favourable and the models with more DOFs are determined to be superior.

Keywords: nonlinear mechanics; buckling; composites.

1. Introduction

Sandwich construction is a popular provider of structural strength combined with weight efficiency which is used extensively in astronautic (Kodiyalam *et al.*, 1996), aeronautic (Bannink *et al.*, 1978; Duthie, 1987), marine (Knox *et al.*, 1998) and in civil engineering applications (Østergaard, 2008). However, precisely because it is both specialized and efficient, the response under certain types of loading is liable to exhibit complicated collapse mechanisms (Hunt *et al.*, 1988; Hunt & Wadee, 1998; Sokolinsky & Frostig, 1999). It is well known from the work of Allen (1969) that compressed sandwich panels sometimes fail by a combination of overall (Euler) buckling and local buckling (wrinkling) of the face plates.

Previous work on sandwich struts under pure compression has revealed different stages in the loading history. Initially, pure squashing is observed followed by Euler buckling that proceeds to interactive buckling where the structure becomes unstable (Fig. 1) and localization is clearly observed (Wadee, 1999). This type of structural response has been modelled analytically using a combination of nonlinear structural stability and Timoshenko beam (TBT) theories that allows the development of shear strains within the core material. These shear strains are vital in the nonlinear interaction of the overall buckling wavelength scale and the local buckling 'strut on elastic foundation' wavelength scale (Hunt & Wadee, 1998). Further work on interactive buckling in sandwich struts considered sensitivity to imperfections (Wadee, 2000), face–core delamination (Wadee & Blackmore, 2001; Wadee, 2002) and

†Present address: Department of Civil Engineering, School of Engineering and Design, Brunel University, Uxbridge UB83PH, UK.

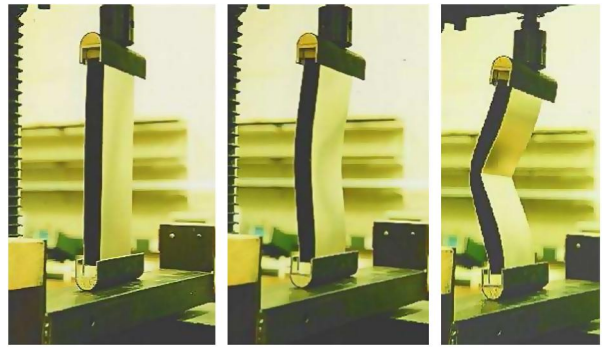

FIG. 1. Photographs of an experimental sandwich panel under axial compression (Wadee, 1999). From left to right: pre-buckling followed by overall buckling and subsequent interaction between overall and local buckling modes leading to localization.

struts with differing face plate thicknesses (Wadee & Simões da Silva, 2005). Recently, the mechanical model of the sandwich struts was improved further by implementing a higher order bending theory, the so-called Reddy–Bickford Theory (RBT), which releases the constraint of plane cross sections remaining plane and allows nonlinear in-plane deformations to develop in the core. This formulation was validated using a finite element (FE) model exhibiting excellent agreement with the post-buckling response and corresponding deformations (Wadee *et al.*, 2010).

In spite of significant progress, these works have focused only on the pure compression case. The work by Wadee & Simões da Silva (2005) on panels with differing face plate geometries highlighted the sensitivity to initial imperfections in geometry but with the limiting requirement that the axial loading acts precisely along the neutral axis. The current study releases this constraint by allowing the axial load to be offset from the neutral axis, hence converting the strut into a member that combines axial loads with uniform bending, a so-called 'beam-column'. Earlier works on beam-columns (Drysdale *et al.*, 1979; Fazio *et al.*, 1982) provided information on critical loads and deflected shapes; the current work extends this to include nonlinear interactive buckling. Since this type of loading is relatively common in practice, the current work gives designers further valuable information on the residual strength capacity after any structural instabilities have occurred.

The current paper begins with the adaptation of the two strut models, one for TBT and the other for RBT, described in Wadee *et al.* (2010), to take into account the change in the work done due to the eccentric axial force. Two further submodels are developed, where the effect of pure bending is taken into consideration in the displacement functions for the overall behaviour. The models are formulated analytically and the resulting governing equations are solved numerically using AUTO97 (Doedel *et al.*, 1997) for a number of panels with different properties. The resulting equilibrium paths and corresponding deformations are presented with discussions of the destabilizing effects and are validated using a fully numerical model created with the commercial general purpose FE package ABAQUS (2006). Conclusions are then drawn.

2. Analytical modelling

The formulation for a simply supported sandwich beam-column panel under axial loading applied offset from the panel neutral axis is presented. The panel is modelled as two thin face plates with Young's modulus E and Poisson's ratio ν separated by a soft linear elastic and orthotropic core material of Young's moduli E_x and E_y with respective Poisson's ratios ν_x and ν_y, shear modulus G_c and the dimensions

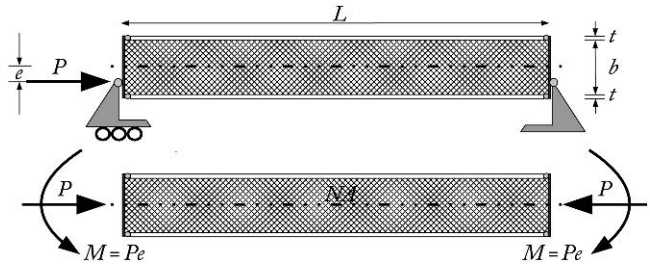

FIG. 2. The sandwich panel in elevation and cross section, 'NA' represents the panel's neutral axis for bending. The lower diagram shows the equivalent combination of axial load P and external moment M.

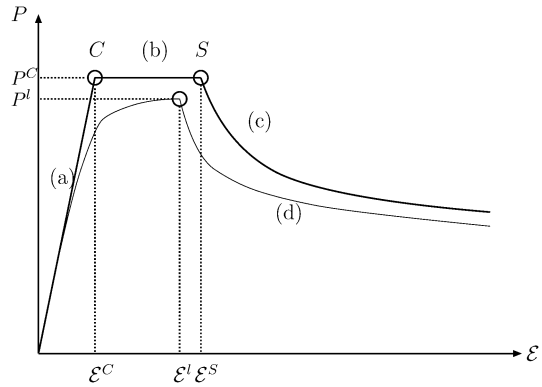

FIG. 3. Equilibrium paths of load P versus end-shortening $\mathcal{E}$. Paths (a)–(c) apply to the sandwich strut only with path (d) for the beam-column only. (a) Initial pure squash fundamental path F to the critical point C; (b) overall buckling path to the secondary bifurcation S; (c) path of interactive buckling; (d) represents the equilibrium path with the single bifurcation point marking the onset of interactive buckling.

shown in Fig. 2. If P is acting at mid-depth, then the force is coincident with the panel neutral axis for bending and reflects the purely axial problem. In that case, the equilibrium path is expected to consist of three clear stages: the pure squash fundamental path F as shown in Fig. 3(a) until a critical load P^{C} is reached beyond which buckling in the overall mode is observed as shown in Fig. 3(b). Finally, this is followed by a secondary bifurcation S in which the face plate under greater compression buckles in a localized mode leading to a highly unstable post-buckling response as shown in Fig. 3(c). The analysis of the purely axial loading case was originally addressed by Hunt & Wadee (1998).

As the applied force moves away from the neutral axis ($e \neq 0$) towards one of the two face plates, end moments are initiated that provide a bias for the overall buckling mode since one face plate becomes more compressed than the other. This eccentricity e transforms the equilibrium path of the structure to a one with a single point of instability that still bears the hallmarks of a pitchfork bifurcation problem (Glendinning, 1994). This new path has a reduced limiting load P^l, below the critical load for the pure strut P^{C}, with increasing eccentricity as sketched in Fig. 3(d).

2.1 *Displacement functions and generalized coordinates*

The deformation system of the model is described through displacement functions and generalized co-ordinates, which are shown in Fig. 4 and discussed below. The displacement functions are utilized to

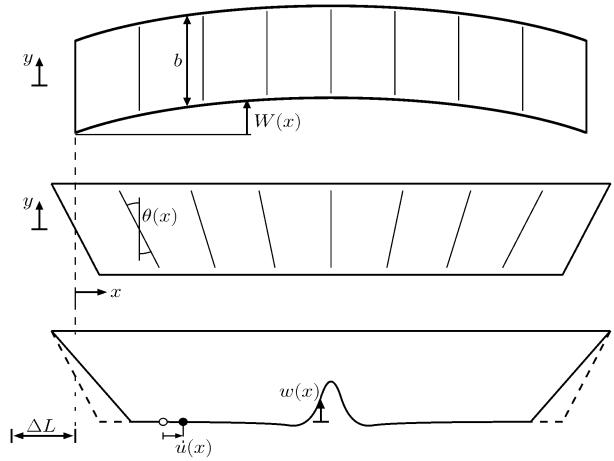

FIG. 4. Top: overall sway mode $W(x)$; middle: overall tilt mode $\theta(x)$; bottom: local modes $u(x)$ and $w(x)$ becoming non-zero beyond the second bifurcation.

formulate the total potential energy V that is subsequently minimized with respect to the generalized coordinates, yielding the governing equations. Beginning with the overall mode, this is decomposed into independent "sway" and "tilt" components to allow for the development of shear strains in the core:

$$W(x) = q_{\mathrm{s}} L \sin \frac{\pi x}{L}, \quad \theta(x) = q_{\mathrm{t}} \pi \cos \frac{\pi x}{L}, \tag{1}$$

where q_{s} and q_{t} are the dimensionless generalized coordinates that describe the amount of sway and tilt, respectively. Generally, shorter wavelength secondary buckling is described by two functions $u(x)$ and $w(x)$, for the in-plane and transverse displacements, respectively, of the more compressed face plate. Allowing these two functions to remain initially unknown, they are free to choose their minimum energy configuration. In the core, both u_{c} and w_c vary linearly in y to zero at the top, less compressed face plate:

$$u_{\mathrm{c}}(x, y) = \left(\frac{b - 2y}{2b}\right) u(x), \quad w_{\mathrm{c}}(x, y) = \left(\frac{b - 2y}{2b}\right) w(x). \tag{2}$$

The linear distribution is kept even though for one of the bending models discussed below, a nonlinear displacement field through the depth of the core is assumed. Sensitivity studies conducted during the numerical investigation suggested that a nonlinear distribution in y did not change the numerical results significantly. Finally, the quantity Δ is the generalized coordinate accounting for the compression along the neutral axis of the panels due to the application of axial load, and its major role is to allow for pre-buckling compression. Moreover, in the post-buckling range Δ allows for some of the compression to be released into bending displacements and therefore gives a measure of the average end compression during the nonlinear buckling process.

2.2 *Energy formulation*

The current paper initially presents two mechanical models with different bending theories. The first one, developed by Hunt & Wadee (1998), is based on a TBT approach that allows the development of

constant shear strains across the depth of the beam. Using a similar philosophy, Wadee *et al.* (2010) relaxed the constant shear condition by utilizing the higher order Reddy–Bickford bending theory (Reddy, 1984, 1990), which is more applicable for deeper beams since it allows for the development of nonlinear (cubic) in-plane deformations in the core. The potential energy V for each of the two models is presented currently highlighting the differences. Henceforth, the abbreviation 'TBT' will be used to refer to the model based on the one presented in Hunt & Wadee (1998), while 'RBT' will refer to the more recent model based on the one presented in Wadee *et al.* (2010). As far as the deformation fields of each model are concerned, the vertical deflections $W(x)$ are the same, whereas the difference lies in the overall in-plane deflection u_g:

$$u_{g,\mathrm{T}}(x,y) = -y\theta(x), \quad u_{g,\mathrm{R}}(x,y) = -y\theta(x) - \frac{4y^3}{3b^2}(\ddot{W} - \dot{\theta}), \tag{3}$$

where the cubic dependence on y is obvious for the RBT model. Note that subscripts T and R refer to the TBT and RBT models, respectively, and dots denote differentiation with respect to x. The total potential energy of the systems consists of the strain energy stored in the sandwich panel minus the work done by the loads, integrated over the volume of the structure. The strain energy has three components of which two are for the face plates in terms of bending energy, U_b and membrane energy, U_m. The third component concerns the strain energy stored in the core and consists of contributions from axial, transverse and shear strains U_c. The work done by the loads include the usual component from the axial load P and a new component from the induced end moment M. The derivation of the total potential energy is given in detail below for both bending models.

2.2.1 *Bending energy.* The bending energy arises from the overall bending of both face plates and a contribution from the local bending of the more compressed face plate due to local buckling. The expression is the same for both TBT and RBT models:

$$U_\mathrm{b} = \frac{EI}{2}\int_0^L (2\ddot{W}^2 + \ddot{w}^2)\,\mathrm{d}x, \tag{4}$$

where EI is the flexural rigidity of one face plate about its local minor axis of bending, hence $EI = Ect^3/[12(1-\nu^2)]$.

2.2.2 *Membrane energy.* The membrane energy U_m accounts for the axial tension and compression in the face plates. Assuming the sandwich panel bends or buckles upwards, the top face plate contributes the axial tensile strain minus the squash term. Similarly, the bottom face plate contributes the compressive axial strain, the squash component and extra contributions from von Kármán large-deflection plate theory to account for any deviation from the overall mode. Since the two models have different in-plane deformation fields in the overall mode, the axial strains for each model would be different. The expression for membrane energy is:

$$U_\mathrm{m} = D\int_0^L (\varepsilon_{xt}^2 + \varepsilon_{xb}^2)\,\mathrm{d}x, \tag{5}$$

where $D = Etc/2$. The axial strains for the face plates are given below. For TBT:

$$\varepsilon_{xt,\mathrm{T}} = -\frac{b}{2}\dot{\theta} - \Delta, \quad \varepsilon_{xb,\mathrm{T}} = \frac{b}{2}\dot{\theta} - \Delta + \dot{u} + \frac{1}{2}\dot{w}^2. \tag{6}$$

For RBT, some extra terms are introduced due to the nonlinear deformation field:

$$\varepsilon_{xt,\mathrm{R}} = -\frac{b}{2}\dot{\theta} - \frac{b}{6}(\ddot{W} - \dot{\theta}) - \Delta, \quad \varepsilon_{xb,\mathrm{R}} = \frac{b}{2}\dot{\theta} + \frac{b}{6}(\ddot{W} - \dot{\theta}) - \Delta + \dot{u} + \frac{1}{2}\dot{w}^2. \tag{7}$$

Hence, the total membrane energy for TBT ($U_{\mathrm{m,T}}$) is given by substituting the expressions for $\varepsilon_{xt,\mathrm{T}}$ and $\varepsilon_{xb,\mathrm{T}}$ for ε_{xt} and ε_{xb}, respectively, into (5). Similarly, for the RBT model, the membrane energy ($U_{\mathrm{m,R}}$) is given by substituting the expressions for $\varepsilon_{xt,\mathrm{R}}$ and $\varepsilon_{xb,\mathrm{R}}$ for ε_{xt} and ε_{xb}, respectively, into (5).

2.2.3 *Core energy.* The core is assumed to behave as a 2D orthotropic elastic solid. The core strain energy U_{c} consists of contributions from axial, transverse and shear strains integrated over its volume:

$$U_{\mathrm{c}} = \int_0^L \int_{-b/2}^{b/2} \left[\frac{c}{2(1-\nu_x\nu_y)}(E_x\varepsilon_x^2 + E_y\varepsilon_y^2 + 2\nu_x E_y\varepsilon_x\varepsilon_y) + G_c c\gamma_{xy}^2 \right] \mathrm{d}y\, \mathrm{d}x. \tag{8}$$

The transverse strain ε_y is the same for both models:

$$\varepsilon_y = \nu_x \Delta + \frac{\partial w_c}{\partial y}, \tag{9}$$

where the first term removes some spurious terms due to the presence of the $\varepsilon_x\varepsilon_y$ term in U_{c}. The axial and shear strains differ for the two bending models because of differences in the deformation field:

$$\varepsilon_{x,\mathrm{T}} = -y\dot{\theta} - \Delta + \dot{u}_c + \frac{1}{2}\dot{w}_c^2, \quad \gamma_{xy,\mathrm{T}} = \dot{W} - \theta + \dot{w}_c + \frac{\partial u_{\mathrm{c}}}{\partial y}, \tag{10}$$

$$\varepsilon_{x,\mathrm{R}}(x,y) = -y\dot{\theta} - \frac{4y^3}{3b^2}(\ddot{W} - \dot{\theta}) - \Delta + \dot{u}_c + \frac{1}{2}\dot{w}_c^2, \quad \gamma_{xy,\mathrm{R}} = \dot{W} + \frac{\partial u_g}{\partial y} + \dot{w}_c + \frac{\partial u_{\mathrm{c}}}{\partial y}. \tag{11}$$

Hence, the total core energy for TBT ($U_{\mathrm{c,T}}$) is given by substituting the expressions for $\varepsilon_{x,\mathrm{T}}$ and $\gamma_{xy,\mathrm{T}}$ for ε_x and γ_{xy}, respectively, into equation (8). Similarly, for the RBT model, the core energy ($U_{\mathrm{c,R}}$) is given by substituting the expressions for $\varepsilon_{x,\mathrm{R}}$ and $\gamma_{xy,\mathrm{R}}$ for ε_x and γ_{xy}, respectively, into equation (8).

2.2.4 *Work done and total potential energy.* The work done contribution has two components: one accounts for the direct action of the axial load P and the other accounts for the external moment M introduced by the eccentricity of the axial load such that $M = Pe$. The work done by the axial load is defined by the load multiplied by the corresponding end shortening $\mathcal{E}$, while for the moment it is defined as M multiplied by the corresponding end rotation Θ. The work done expression is the same for both models due to their identical boundary conditions:

$$P\mathcal{E} + M\Theta = \int_0^L P\left[\left(\frac{1}{2}q_s^2\pi^2\cos^2\frac{\pi x}{L} - \frac{1}{2}\dot{u} + \Delta\right) + e\left(2q_t\frac{\pi}{L} - \frac{\dot{u}}{b}\right)\right] \mathrm{d}x. \tag{12}$$

The potential energy functions for each model are given below:

$$V_{\mathrm{T}} = U_{\mathrm{b}} + U_{\mathrm{m,T}} + U_{\mathrm{c,T}} - (P\mathcal{E} + M\Theta), \tag{13}$$

$$V_{\mathrm{R}} = U_{\mathrm{b}} + U_{\mathrm{m,R}} + U_{\mathrm{c,R}} - (P\mathcal{E} + M\Theta). \tag{14}$$

The detailed expressions for V, the pure compression cases can be found in Wadee & Hunt (1998) for the TBT case, and Wadee *et al.* (2010) for the RBT case. The only real change being caused by the inclusion of the Mq_t term in the work done, which essentially changes the problem from a two bifurcation point problem to a single bifurcation point problem with a non-trivial fundamental path that introduces uniform bending before the instability. For clarity, henceforth, some material and geometric constants have been grouped together such that:

$$G = \frac{G_c bc}{2}, \quad C_x = \frac{E_x bc}{2(1-\nu_x\nu_y)}, \quad C_y = \frac{E_y bc}{2(1-\nu_x\nu_y)}, \quad k = \frac{2C_y}{b^2}, \quad \phi = \frac{b}{L}. \tag{15}$$

It is worth noting that the coefficients in the membrane strain terms of the bottom face plate in (6) and (7) concerned with the overall mode, and the lower limit of integration for y in (8), could be altered to include w. This would have the effect of incorporating the change in the depth of the cross section that would occur with the introduction of localized buckling of the bottom face plate. Moreover, local deformations in the top face plate also resulting from the interactive buckling process could also be included to reflect the physical behaviour more accurately. To achieve this, two additional displacement functions similar to w and u, defined above, would be necessary for the top face plate, which would in turn introduce two further ordinary differential equations (ODEs), probably a fourth order and a second order, respectively, into the system. The introduction of more nonlinear terms and displacement functions, which would naturally occur as a result of these additional features being incorporated, would not have a significant effect until the local deflections become very large at which stage other important sources of nonlinearity, such as from within the core (Hunt & Wadee, 1998; Gibson & Ashby, 1999) and from plasticity, would also take hold. However, inclusion of these aspects would have the effect of complicating the model considerably without commensurate gain in practical information; hence, they are not incorporated currently and are left for future work.

2.2.5 *Linear eigenvalue analysis for overall buckling.* The critical buckling load for each model for the pure compression case ($M = 0$) can be obtained through linear eigenvalue analysis as described in Hunt & Wadee (1998):

$$\begin{aligned} P_{\mathrm{T}}^{\mathrm{C}} &= \frac{2\pi^2 EI}{L^2} + 2G\pi^2\phi^2\left[\frac{\left(D+\frac{C_x}{6}\right)}{2G+\phi^2\pi^2\left(D+\frac{C_x}{6}\right)}\right], \\ P_{\mathrm{R}}^{\mathrm{C}} &= \frac{2\pi^2 EI}{L^2} + \frac{840G\pi^2\phi^2(C_x+6D)+C_x\pi^4\phi^4(C_x+20D)}{30(168G+17C_x\phi^2\pi^2+70D\phi^2\pi^2)}. \end{aligned} \tag{16}$$

The first terms in each expression relate to the load of the face plates buckling independently. The other terms consist of the contributions from the face plates bending about the global neutral axis of the panel. The RBT critical load ($P_{\mathrm{R}}^{\mathrm{C}}$) is always marginally greater than the TBT critical load ($P_{\mathrm{T}}^{\mathrm{C}}$) since the nonlinear in-plane strain distribution increases the threshold for buckling. Both expressions, however, closely agree with the classical result of Allen (1969) for panels with thin face plates and relatively weak cores.

2.2.6 *Governing equations.* The total potential energy V, whether it is equal to V_{T} or V_{R}, is an integral with $\mathcal{L}$ being the integrand. For equilibrium to be satisfied, the total potential energy must be

stationary which requires the first variation of V, δV, where

$$\delta V = \int_0^L \left(\frac{\partial \mathcal{L}}{\partial \ddot{w}} \delta \ddot{w} + \frac{\partial \mathcal{L}}{\partial \dot{w}} \delta \dot{w} + \frac{\partial \mathcal{L}}{\partial w} \delta w + \frac{\partial \mathcal{L}}{\partial \dot{u}} \delta \dot{u} + \frac{\partial \mathcal{L}}{\partial u} \delta u \right) \mathrm{d}x, \tag{17}$$

to vanish (Fox, 1987). Following the procedure of applying the calculus of variations presented in Hunt & Wadee (1998) involving integrating by parts to minimize V for all δw and δu, it turns out that pinned supports are acceptable boundary conditions, where the local lateral deflection and curvature at the ends, *i.e.* $w(0)$, $w(L)$, $\ddot{w}(0)$ and $\ddot{w}(L)$ are zero. Moreover, the following in-plane boundary conditions are also given:

$$2\dot{u}(x_0)\left(D + \frac{C_x}{3}\right) + \dot{w}^2(x_0)\left(D + \frac{C_x}{4}\right) = \Delta[2D + C_x - C_y(1 - \nu_x^2)] - \frac{P}{2} - \frac{M}{b}, \tag{18}$$

where $x_0 = 0$ and $x_0 = L$; physically, this can be obtained by matching the strains from the loads at the ends. Subject to the above boundary conditions, the condition $\delta V = 0$ is satisfied by the Euler–Lagrange equations that yield two coupled nonlinear ODEs, a fourth order ODE in w and a second order ODE in u. Moreover, when V is minimized with respect to the three generalized coordinates q_s, q_t and Δ, three further equilibrium equations are determined that connect the generalized coordinates to the displacement functions. Note that there is nothing particularly special in the terms in braces with subscripts T and R in the following equations, apart from that the expressions that they are equal to, on their right-hand side, are reused for conciseness in Section 4.2. The system of equations for the TBT model is presented first:

$$\begin{aligned}\{EI\ddot{w}\}_\mathrm{T} = &-D\left[2\Delta\ddot{w} + q_\mathrm{t}\phi\pi^2\left(\sin\frac{\pi x}{L}\ddot{w} + \frac{\pi}{L}\cos\frac{\pi x}{L}\dot{w}\right) - (2\dot{u}\ddot{w} + 2\ddot{u}\dot{w} + 3\dot{w}^2\ddot{w})\right] \\ &- C_x\left[\frac{2}{3}\Delta\ddot{w} - \left(\frac{1}{2}\ddot{u}\dot{w} + \frac{1}{2}\dot{u}\ddot{w} + \frac{3}{5}\dot{w}^2\ddot{w}\right) + q_\mathrm{t}\frac{\phi\pi^2}{6}\left(\sin\frac{\pi x}{L}\ddot{w} + \frac{\pi}{L}\cos\frac{\pi x}{L}\dot{w}\right)\right] - kw \\ &- \frac{C_y\nu_x}{b}\left[\frac{2}{3}w\ddot{w} - \frac{2}{3}\nu_x\Delta b\ddot{w} - \left(\dot{u} - \frac{1}{3}\dot{w}^2\right)\right] - G\left[\frac{\dot{u}}{b} - \frac{2}{3}\ddot{w} + (q_\mathrm{s} - q_\mathrm{t})\frac{\pi^2}{L}\sin\frac{\pi x}{L}\right],\end{aligned} \tag{19}$$

$$\begin{aligned}\left\{2\ddot{u}\left(D + \frac{C_x}{3}\right)\right\}_\mathrm{T} = &-\frac{G}{b}\left(\frac{\dot{w}}{2} - \frac{u}{b}\right) - \left(D + \frac{C_x}{4}\right)\dot{w}\ddot{w} - \frac{C_y\nu_x}{2b}\dot{w} \\ &-\frac{\pi}{b}\cos\frac{\pi x}{L}\left[G(q_\mathrm{s} - q_\mathrm{t}) - \left(D + \frac{C_x}{6}\right)\frac{\pi^2\phi^2}{2}q_\mathrm{t}\right],\end{aligned} \tag{20}$$

$$\{P\}_\mathrm{T} = \frac{2\pi^2 EI}{L^2} + \frac{2G}{q_\mathrm{s}}\left[(q_\mathrm{s} - q_\mathrm{t}) + \frac{1}{\pi L}\int_0^L \cos\frac{\pi x}{L}\left(\dot{w} - \frac{2u}{b}\right)\mathrm{d}x\right], \tag{21}$$

$$\begin{aligned}\left\{\frac{M}{b}\right\}_\mathrm{T} = &\frac{G\pi}{2\phi}(q_\mathrm{t} - q_\mathrm{s}) + \left(\frac{C_x}{6} + D\right)\frac{\phi\pi^3}{4}q_\mathrm{t} \\ &-\frac{1}{L}\int_0^L \left[\left(D + \frac{C_x}{6}\right)\frac{\pi}{2}\sin\frac{\pi x}{L}\left(\dot{u} + \frac{\dot{w}^2}{2}\right) + \frac{G}{2\phi}\cos\frac{\pi x}{L}\left(\dot{w} - \frac{2u}{b}\right)\right]\mathrm{d}x,\end{aligned} \tag{22}$$

$$\frac{P}{2} = \Delta(2D + C_x - C_y\nu_x^2) - \frac{D}{L}\int_0^L \left[\left(\dot{u} + \frac{1}{2}\dot{w}^2\right) + \left(\frac{C_x - C_y\nu_x^2}{2D}\right)\left(\dot{u} + \frac{1}{3}\dot{w}^2\right)\right] \mathrm{d}x. \tag{23}$$

The following system of equations is derived from the RBT formulation, with the equilibrium equation, $\partial V_{\mathrm{R}}/\partial \Delta = 0$, being the same as (23):

$$\begin{aligned}\{EI\ddot{w}\}_{\mathrm{R}} = &-D\left[2\Delta\ddot{w} + (2q_{\mathrm{t}} + q_{\mathrm{s}})\frac{\phi\pi^2}{3}\left(\sin\frac{\pi x}{L}\ddot{w} + \frac{\pi}{L}\cos\frac{\pi x}{L}\dot{w}\right) - (2\dot{u}\ddot{w} + 2\ddot{u}\dot{w} + 3\dot{w}^2\ddot{w})\right] \\ &- C_x\left[\frac{2}{3}\ddot{w} - \frac{3}{5}\dot{w}^2\ddot{w} - \frac{1}{2}(\dot{w}\ddot{u} + \ddot{w}\dot{u}) + (q_{\mathrm{s}} + 4q_{\mathrm{t}})\frac{\phi\pi^2}{30}\left(\sin\frac{\pi x}{L}\ddot{w} + \frac{\pi}{L}\cos\frac{\pi x}{L}\dot{w}\right)\right] - kw \\ &- \frac{C_y}{b}\nu_x\left\{\frac{2}{3}[\ddot{w}\,(w - \nu_x\Delta b)] - \left(\dot{u} - \frac{1}{3}\dot{w}^2\right) + G\left[\frac{2}{3}\ddot{w} - \frac{\dot{u}}{b} - (q_{\mathrm{s}} - q_{\mathrm{t}})\frac{2\pi^2}{3L}\sin\frac{\pi x}{L}\right]\right\},\end{aligned} \tag{24}$$

$$\begin{aligned}\left\{2\ddot{u}\left(D + \frac{C_x}{3}\right)\right\}_{\mathrm{R}} = &\frac{C_y}{b}\nu_x\dot{w} - D\left[2\dot{w}\ddot{w} - (q_{\mathrm{s}} + 2q_{\mathrm{t}})\frac{\phi\pi^3}{3L}\cos\frac{\pi x}{L}\right] \\ &- C_x\left[\frac{1}{2}\dot{w}\ddot{w} - \frac{\phi\pi^3}{30L}(q_{\mathrm{s}} + 4q_{\mathrm{t}})\cos\frac{\pi x}{L}\right] - \frac{G}{b}\left[\dot{w} + \frac{4}{3\pi}(q_{\mathrm{s}} - q_{\mathrm{t}})\cos\frac{\pi x}{L} - \frac{2u}{b}\right],\end{aligned} \tag{25}$$

$$\begin{aligned}\{P\}_{\mathrm{R}} = &\frac{2\pi^2 EI}{L^2} + \frac{16G}{15}\left(1 - \frac{q_{\mathrm{t}}}{q_{\mathrm{s}}}\right) + \frac{D\phi^2\pi^2}{9}\left(1 + \frac{2q_{\mathrm{t}}}{q_{\mathrm{s}}}\right) + \frac{C_x\phi^2\pi^2}{126}\left(1 + \frac{5q_{\mathrm{t}}}{q_{\mathrm{s}}}\right) \\ &+ \frac{1}{q_{\mathrm{s}}L}\int_0^L \left[\frac{4G}{3\pi}\cos\frac{\pi x}{L}\left(\dot{w} - \frac{2u}{b}\right) - \frac{\phi}{15}(10D + C_x)\sin\frac{\pi x}{L}\left(\dot{u} + \frac{1}{2}\dot{w}^2\right)\right]\mathrm{d}x,\end{aligned} \tag{26}$$

$$\begin{aligned}\left\{\frac{M}{b}\right\}_{\mathrm{R}} = &\frac{G\pi}{2\phi}(q_{\mathrm{t}} - q_{\mathrm{s}}) + \frac{\phi\pi^3}{630}[q_{\mathrm{s}}(35D + 4C_x) + q_{\mathrm{t}}(70D + 17C_x)] \\ &- \frac{1}{L}\int_0^L \left[\left(D + \frac{C_x}{5}\right)\frac{\pi}{3}\sin\frac{\pi x}{L}\left(\dot{u} + \frac{1}{2}\dot{w}^2\right) + \frac{G}{3\phi}\cos\frac{\pi x}{L}\left(\dot{w} - \frac{2u}{b}\right)\right]\mathrm{d}x.\end{aligned} \tag{27}$$

The equilibrium equation, $\partial V/\partial q_{\mathrm{t}} = 0$, highlights the principal difference from the strut model since it includes the external moment term. This transforms the previously linear fundamental path followed by a pitchfork bifurcation for the pure compression case, to a nonlinear fundamental path for the beam-column (Fig. 3d) followed by a bifurcation point. In both cases, localized buckling is triggered when the stress in the more compressed face plate exceeds its local buckling capacity.

3. Preliminary results: 2 degrees of freedom models

The systems of equations are solved using the numerical continuation package AUTO97 (Doedel *et al.*, 1997) for different load eccentricities. AUTO is a numerical continuation package that is primarily designed to solve systems of autonomous ODEs and to provide information on how the solutions evolve

with parametric changes. However, it is also capable of solving non-autonomous ODEs (as in the current study), initial value problems, boundary value problems, systems of algebraic equations and to a small extent, systems of parabolic partial differential equations. It is particularly well known for its capability to locate bifurcation points of many different types including: saddle–node, pitchfork, period doubling, torus and Hopf; it is also capable of tracing out multiple branching paths and switching between them. Furthermore, it has the capability of computing homoclinic orbits. In the current study, it is used as a boundary value problem solver for a system of two non-autonomous ODEs subject to integral conditions and it is the same software that was utilized for the pure strut problem (Hunt & Wadee, 1998; Wadee *et al.*, 2010) with excellent results. Owing to the symmetry of the structural boundaries of the problem, to reduce computational cost, the equations are solved for half of the panel by applying symmetry conditions:

$$\dot{w}(L/2) = \dddot{w}(L/2) = u(L/2) = 0. \tag{28}$$

Naturally, these conditions exclude the possibility of any asymmetric solutions for w but it has been seen in previous studies (Wadee, 2000) for the strut problem that the symmetric localized solution has the absolute minimum critical load for cases where the overall buckling mode wavelength is significantly larger than that of the local buckling mode; practical engineering geometries satisfy this condition. The following material and geometric properties for the sandwich panels are used in the case study:

Face plate Young's modulus:	$E = 68900\ \mathrm{N/mm^2}$
Face plate Poisson's ratio:	$\nu = 0.3$
Face plate thickness:	$t = 0.5$ mm
Core Young's modulus (in x and y):	$E_x = E_y = 199\ \mathrm{N/mm^2}$
Core Poisson's ratio (in x and y):	$\nu_x = \nu_y = 0.2$
Core Shear modulus:	$G_c = 83\ \mathrm{N/mm^2}$
Core depth (range):	$b = 5.1\ \mathrm{mm} \rightarrow 10.2\ \mathrm{mm}$
Strut length:	$L = 100$ mm
Load eccentricity ratio (range):	$e/b = 0.1 \rightarrow 0.5$.

The load eccentricity ratio e/b is considered only up to the physical limit of 0.5, where the load is effectively acting directly on the face–core interface. Equilibrium paths and buckling modes of the panels under different eccentricities are presented below.

3.1 *Equilibrium paths and buckling modes*

The first sandwich panel to be investigated had a core depth $b = 5.1$ mm and the load was applied at various e/b ratios. As expected from previous work for the strut problem, the two models have a similar initial pre-buckling path until the point of instability was reached. The increase in the e/b ratio produces shallower and less stiff paths that deviate further from the pure strut case (Fig. 5). The limiting loads for the RBT model are always higher than the TBT limiting loads, drawing parallels with the pure strut problem (Wadee *et al.*, 2010). However, the limiting loads in both models decrease with increasing eccentricity at an almost identical rate (Fig. 6(a)). As in the pure strut case, the membrane stresses developed for the RBT model in the bottom face plate exceed the threshold for plate buckling earlier than the TBT model, leading to the earlier initiation of interactive buckling for the RBT case.

An interesting feature in the results was found during the comparison of the evolution of the overall mode components, sway and tilt. Fig. 6(b) shows q_t plotted against q_s for loads applied at various eccentricities ($e/b = 0.1$, 0.3 and 0.5). During pre-buckling, the two models exhibit similar trends

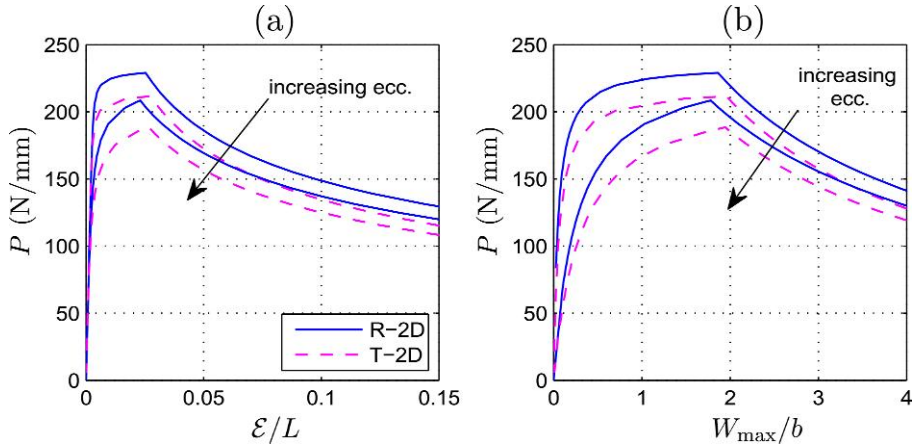

FIG. 5. Equilibrium paths for struts with eccentricities $e/b = 0.1$ and 0.5. (a) Load versus normalized end shortening and (b) load versus maximum lateral deflection.

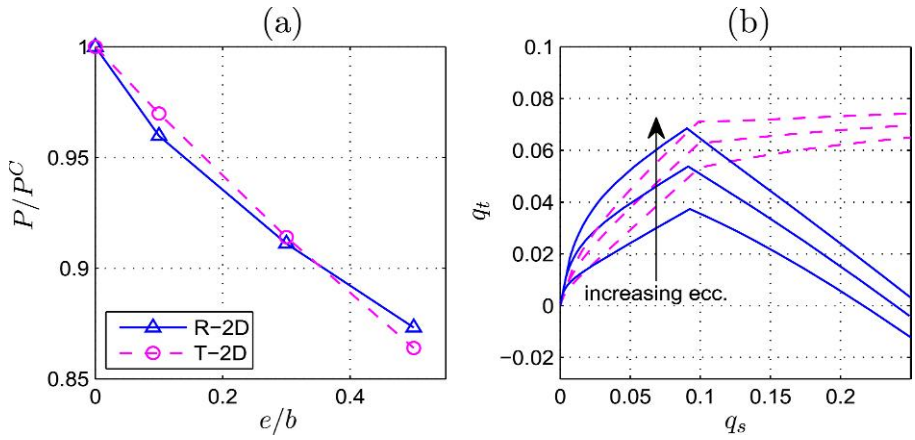

FIG. 6. (a) The decrease of limiting loads with increasing eccentricity, (b) the evolution of the generalized coordinates along the equilibrium paths for $e/b = 0.1$ (lowest values of q_t) 0.3 and 0.5.

with q_t increasing along with q_s. Beyond the point of instability, for the TBT model, the slope of q_t decreases abruptly indicating a slower growth with increasing q_s. On the other hand, in the RBT model the slope of the response beyond the instability becomes negative; hence, q_t decreases with increasing q_s. This difference in the response can be attributed to the nonlinear (cubic) cross-sectional deformation field that relaxes the constraint of constant tilting throughout the depth of the panel. Before the point of instability, the difference in the cross-sectional deformations are small (Fig. 7); beyond it, the in-plane displacement within the core becomes increasingly nonlinear while the displacement at the edges is very close to the corresponding displacements of the TBT models. The decrease in q_t occurs as the minimum energy configuration for this displacement field is significantly influenced by the flexibility of the core under shear.

Localized buckling is triggered at the bifurcation point and the modes are similar for both current models and the strut case ($M = 0$) since this is caused by the compressive stresses in the bottom

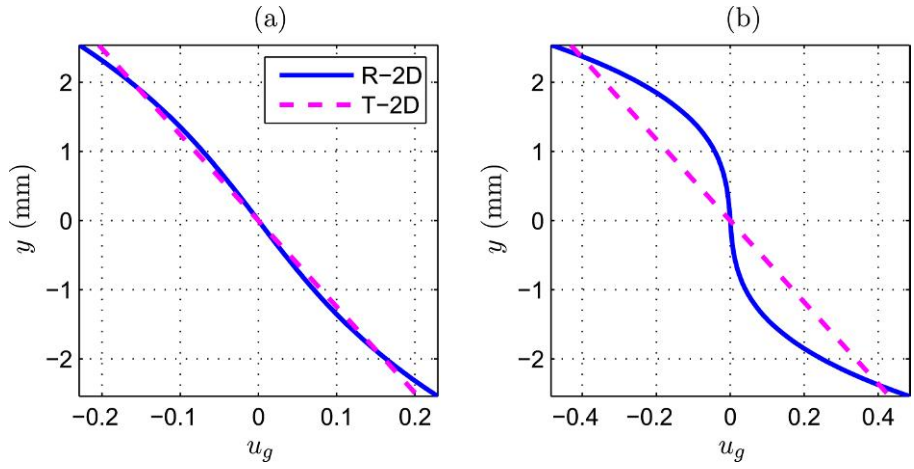

FIG. 7. In-plane deformations for $b = 5.1$ mm and $e/b = 0.3$ at $x = L/6$. (a) Before ($q_s = 0.05$) and (b) after ($q_s = 0.15$) the point of instability.

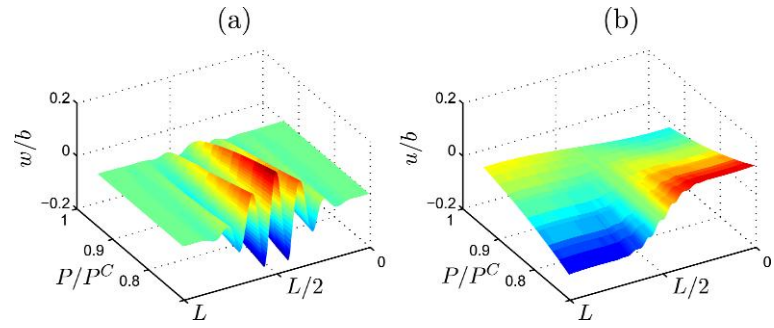

FIG. 8. The evolution of localized modes (a) w and (b) u. Plotted for the case where $b = 5.1$ mm and $e/b = 0.2$.

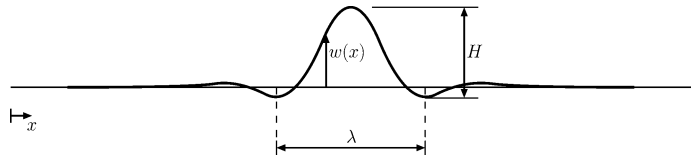

FIG. 9. Definition of localized buckle wavelength λ and maximum wave height H.

face plate (Fig. 8). The interactive buckling modes of TBT and RBT exhibit similar characteristics qualitatively, having a localized maximum displacement at midspan that decays towards the boundaries. Even though the RBT localized mode is triggered first, leading to a larger mode than the TBT equivalent, particularly in the neighbourhood of the limiting load, the two modes become similar in amplitude and localized wavelength λ (Fig. 9) in the advanced post-buckling range where the sway mode dominates.

4. Submodels with more degrees of freedom

Despite the decrease in the limiting load due to increasing eccentricity, the level of sway at the bifurcation point remains approximately the same for both models since the overall modal displacement functions, W and θ, are not hitherto altered to include the effects of the end moments. The initial response of sandwich beam-columns is not purely squashing but there is also bending that can be decomposed into separate sway and tilt components. Hence, the total potential energy of the panels can be adjusted such that overall bending is explicitly included; more generalized coordinates are henceforth included in W and θ to address this.

When a beam is loaded only with end moments, it is in a state of uniform bending moment which, to first order, can be approximated by a quadratic lateral displacement. Including this alongside the effect of overall buckling, it is expected that the deformation of the beam would be a compromise between the quadratic (bending) and sinusoidal (overall buckling) mode shapes. Moreover, it would be expected that the influence of overall bending would be greater until the bifurcation point, beyond which overall and local buckling would dominate. The changes made to the sway and tilt functions are thus:

$$W(x) = q_{\mathrm{s}} L \sin\frac{\pi x}{L} + q_{\mathrm{sb}} x\left(1 - \frac{x}{L}\right), \quad \theta(x) = q_{\mathrm{t}}\pi \cos\frac{\pi x}{L} + q_{\mathrm{tb}}\left(1 - \frac{2x}{L}\right), \tag{29}$$

where q_{sb} and q_{tb} are the respective sway and tilt amplitudes for the bending mode. These updated modes bring changes with extra terms in the existing equations, besides introducing two further equilibrium equations when V is differentiated with respect to q_{sb} and q_{tb}.

4.1 *Total potential energy*

The total potential energy for the 4 degrees of freedom (DOF) submodels for both bending theories, TBT and RBT, are given below:

$$\begin{aligned} V_{\mathrm{T4}} = \int_0^L \Bigg\{ & 2D\phi q_{\mathrm{tb}}\left[\phi\left(q_{\mathrm{t}}\pi^2 \sin\frac{\pi x}{L} + q_{\mathrm{tb}}\right) - \dot{u} - \frac{1}{2}\dot{w}^2\right] \\ & + \frac{C_x\phi^2}{3} q_{\mathrm{tb}}\left[q_{\mathrm{tb}} + q_{\mathrm{t}}\pi^2 \sin\frac{\pi x}{L} - \frac{1}{\phi}\left(\dot{u} + \frac{1}{2}\dot{w}^2\right)\right] + \frac{4EI}{L^2} q_{\mathrm{sb}}\left(q_{\mathrm{sb}} + q_{\mathrm{s}}\pi^2 \sin\frac{\pi x}{L}\right) \\ & - \frac{P q_{\mathrm{sb}}}{2}\left(1 - \frac{2x}{L}\right)\left[2q_{\mathrm{s}}\pi \cos\frac{\pi x}{L} + q_{\mathrm{sb}}\left(1 - \frac{2x}{L}\right)\right] - \frac{2M q_{\mathrm{tb}}}{L} \\ & + G(q_{\mathrm{sb}} - q_{\mathrm{tb}})\left(1 - \frac{2x}{L}\right)\left[\left(\dot{w} + \frac{2u}{b}\right) + (q_{\mathrm{s}} - q_{\mathrm{t}})\frac{\pi}{2}\cos\frac{\pi x}{L}\right. \\ & \left. + (q_{\mathrm{sb}} - q_{\mathrm{tb}})\left(1 - \frac{2x}{L}\right)\right]\Bigg\} \mathrm{d}x + V_{\mathrm{T}}, \end{aligned} \tag{30}$$

$$\begin{aligned} V_{\mathrm{R4}} = \int_0^L \Bigg\{ & \frac{2D\phi^2}{9}(2q_{\mathrm{tb}} + q_{\mathrm{sb}})\left[2q_{\mathrm{tb}} + q_{\mathrm{sb}} + (2q_{\mathrm{t}} + q_{\mathrm{s}})\pi^2 \sin\frac{\pi x}{L} - \frac{3}{\phi}\left(\dot{u} + \frac{1}{2}\dot{w}^2\right)\right] \\ & - \frac{P q_{\mathrm{sb}}}{2}\left(1 - \frac{2x}{L}\right)\left[2q_{\mathrm{s}}\pi \cos\frac{\pi x}{L} + q_{\mathrm{sb}}\left(1 - \frac{2x}{L}\right)\right] - \frac{2M q_{\mathrm{tb}}}{L} \end{aligned}$$

$$+\frac{C_x\phi^2}{315}\Bigg[68q_{\rm tb}^2+32q_{\rm tb}q_{\rm sb}+5q_{\rm sb}^2-\frac{21}{\phi}(4q_{\rm tb}+q_{\rm sb})\left(\dot u+\frac{1}{2}\dot w^2\right)+(68q_{\rm t}q_{\rm tb}+16q_{\rm t}q_{\rm sb}$$
$$+16q_{\rm tb}q_{\rm s}+5q_{\rm s}q_{\rm sb})\pi^2\sin\frac{\pi x}{L}\Bigg]+\frac{2G(q_{\rm sb}-q_{\rm tb})}{15}\left(1-\frac{2x}{L}\right)\Bigg[4(q_{\rm sb}-q_{\rm tb})\left(1-\frac{2x}{L}\right)$$
$$+5\left(\dot w-\frac{2u}{b}\right)+8\pi(q_{\rm s}-q_{\rm t})\cos\frac{\pi x}{L}\Bigg]+\frac{4EI}{L^2}q_{\rm sb}\left(q_{\rm sb}+q_{\rm s}\pi^2\sin\frac{\pi x}{L}\right)\Bigg\}\,{\rm d}x+V_{\rm R},\tag{31}$$

where $V_{\rm T}$ and $V_{\rm R}$ are given in (13) and (14), respectively.

4.2 *Governing equations*

The systems of equations for the submodels are again derived through the calculus of variations with additional terms in each equation. For the 4-DOF TBT submodel:

$$EI\dddot w=\{EI\dddot w\}_{\rm T}-2\ddot w\phi q_{\rm tb}\,(D+C_x/6)-\frac{2}{L}G(q_{\rm sb}-q_{\rm tb}),\tag{32}$$

$$2\ddot u\left(D+\frac{C_x}{3}\right)=\left\{2\ddot u\left(D+\frac{C_x}{3}\right)\right\}_{\rm T}-\frac{2G}{b}(q_{\rm sb}-q_{\rm tb})\left(1-\frac{2x}{L}\right),\tag{33}$$

$$P=\{P\}_{\rm T}+\frac{8q_{\rm sb}}{\pi^3q_{\rm s}}\left[\frac{2EI\pi^2}{L^2}-P+2G\left(1-\frac{q_{\rm tb}}{q_{\rm sb}}\right)\right],\tag{34}$$

$$\frac{M}{b}=\left\{\frac{M}{b}\right\}_{\rm T}+q_{\rm tb}\left[\frac{4G}{\phi\pi^2}\left(1-\frac{q_{\rm sb}}{q_{\rm tb}}\right)+\frac{2\phi}{\pi}\left(D+\frac{C_x}{6}\right)\right],\tag{35}$$

while $\partial V/\partial\Delta$ is the same as (23). The terms in the braces with the subscript T refer to the expressions on the right-hand side of the respective (19)–(22). The two new equilibrium equations: $\partial V/\partial q_{\rm sb}=0$ and $\partial V/\partial q_{\rm tb}=0$ are, respectively, thus:

$$P(12q_{\rm s}+\pi q_{\rm sb})=\frac{24\pi EI}{L^2}(q_{\rm s}\pi+q_{\rm sb})+G\Bigg[2\pi(q_{\rm sb}-q_{\rm tb})+24\pi(q_{\rm s}-q_{\rm t})$$
$$+\frac{1}{L}\int_0^L\left(1-\frac{2x}{L}\right)\left(\dot w+\frac{2u}{b}\right){\rm d}x\Bigg],\tag{36}$$

$$\frac{M}{b}=2\phi(q_{\rm t}\pi+q_{\rm tb})\left(D+\frac{C_x}{6}\right)+\frac{4G}{\phi}\left[\left(\frac{q_{\rm tb}-q_{\rm sb}}{12}\right)-\left(\frac{q_{\rm s}-q_{\rm t}}{\pi}\right)\right]$$
$$-\frac{1}{L}\int_0^L\left\{\left(\dot u+\frac{1}{2}\dot w^2\right)\left(D+\frac{C_x}{6}\right)+\frac{G}{\phi}\left(1-\frac{2x}{L}\right)\left(\frac{1}{2}\dot w-\frac{u}{b}\right)\right\}{\rm d}x.\tag{37}$$

For the 4-DOF RBT sub-model the new equations are:

$$EI\ddddot{w} = \{EI\ddddot{w}\}_{\mathrm{R}} - \frac{4\phi}{3}\ddot{w}q_{\mathrm{tb}}\left(D + \frac{C_x}{5}\right) - \frac{2\phi}{3}\ddot{w}q_{\mathrm{sb}}\left(D + \frac{C_x}{10}\right) - \frac{4G}{3L}(q_{\mathrm{sb}} - q_{\mathrm{tb}}), \quad (38)$$

$$2\ddot{u}\left(D + \frac{C_x}{3}\right) = \left\{2\ddot{u}\left(D + \frac{C_x}{3}\right)\right\}_{\mathrm{R}} - \frac{4}{3}\frac{G}{b}(q_{\mathrm{sb}} - q_{\mathrm{tb}})\left(1 - \frac{2x}{L}\right), \quad (39)$$

$$P = \{P\}_{\mathrm{R}} + \frac{q_{\mathrm{sb}}}{q_{\mathrm{s}}}\left[\frac{8}{\pi^3}\left(\frac{2EI\pi^2}{L^2} - P\right) + \frac{8D\phi^2}{9\pi}\left(1 + 2\frac{q_{\mathrm{tb}}}{q_{\mathrm{sb}}}\right) + \frac{4C_x\phi^2}{315\pi}\left(5 + 16\frac{q_{\mathrm{tb}}}{q_{\mathrm{sb}}}\right) + \frac{128G}{15\pi^3}\left(1 - \frac{q_{\mathrm{tb}}}{q_{\mathrm{sb}}}\right)\right], \quad (40)$$

$$\frac{M}{b} = \left\{\frac{M}{b}\right\}_{\mathrm{R}} + \frac{32G}{15\phi\pi^2}(q_{\mathrm{tb}} - q_{\mathrm{sb}}) + \frac{4\phi}{315}[q_{\mathrm{tb}}(70D + 17C_x) + q_{\mathrm{sb}}(35D + 4C_x)], \quad (41)$$

with the two new equilibrium equations: $\partial V/\partial q_{\mathrm{sb}} = 0$ and $\partial V/\partial q_{\mathrm{tb}} = 0$ being, respectively:

$$P(12q_{\mathrm{s}} + \pi q_{\mathrm{sb}}) = \frac{24\pi EI}{L^2}(q_{\mathrm{s}}\pi + q_{\mathrm{sb}}) + \frac{16G}{15}[12(q_{\mathrm{s}} - q_{\mathrm{t}}) + \pi(q_{\mathrm{sb}} - q_{\mathrm{tb}})] + \frac{32\phi^2\pi}{105}\left(\frac{35}{4}D + C_x\right)(q_{\mathrm{t}}\pi + q_{\mathrm{tb}}) + \frac{2\phi^2\pi}{21}(14D + C_x)(q_{\mathrm{s}}\pi + q_{\mathrm{sb}}) + \frac{1}{L}\int_0^L \left\{4G\pi\left(\dot{w} - \frac{2u}{b}\right)\left(1 - \frac{2x}{L}\right) - \frac{b}{L}\pi\left(2D + \frac{C_x}{5}\right)\left(\dot{u} + \frac{1}{2}\dot{w}^2\right)\right\} \mathrm{d}x, \quad (42)$$

$$\frac{M}{b} = \frac{4\phi}{315}\{35D[2q_{\mathrm{tb}} + q_{\mathrm{sb}} + \pi(2q_{\mathrm{t}} + q_{\mathrm{s}})] + C_x[17q_{\mathrm{tb}} + 4q_{\mathrm{sb}} + \pi(17q_{\mathrm{t}} + 4q_{\mathrm{s}})]\} + \frac{8G}{45\phi\pi}[(q_{\mathrm{tb}} - q_{\mathrm{sb}})\pi - 12(q_{\mathrm{s}} - q_{\mathrm{t}})] - \frac{2}{15L}\int_0^L \left\{(5D + C_x)\left(\dot{u} + \frac{1}{2}\dot{w}^2\right) + \frac{5G}{2\phi}\left(\dot{w} - \frac{2u}{b}\right)\left(1 - \frac{2x}{L}\right)\right\} \mathrm{d}x. \quad (43)$$

The terms in the braces with the subscript R refer to the expressions on the right-hand side of the respective equations (24)–(27). By taking the second derivative of the five generalized coordinates, setting the terms in the integral to zero and solving the determinant of the Hessian assuming $M = 0$, the same critical loads for the models and submodels of each core bending theory are found. This is not surprising since without the influence of the load eccentricity in the work done, the generalized coordinates of bending (q_{sb} and q_{tb}) do not provide any extra contributions to the critical load. The difference between the 2-DOF models and 4-DOF submodels becomes more pronounced with increasing eccentricity both in terms of lower limiting loads and lower subsequent post-buckling stiffnesses.

5. Numerical comparison of models

All the model equations are again solved using the numerical continuation package AUTO97 (Doedel *et al.*, 1997) subject to the same conditions and symmetry. The two sandwich panels discussed in Section 3 are again utilized for various load eccentricities. In both cases, the 4-DOF submodels have an improved performance compared to their corresponding 2-DOF counterparts in the deformation field by including the influence of pure bending. More importantly, the 4-DOF submodels reduce the limiting loads both in terms of load capacity and with respect to the level of sway at the limiting load. This is as expected with the extra compression in one of the face plates increasing further before any buckling occurs.

5.1 *Equilibrium paths*

The equilibrium paths from all four models for two different cases of load eccentricity ($e/b = 0.1$, 0.5) are given in Fig. 10 for a sandwich panel of depth 5.1 mm. Closer inspection of a case with small eccentricity, $e/b = 0.1$, reveals that the pre-buckling paths for the models of each bending theory are almost identical. However, the bifurcation point occurs earlier with a slightly lower load level for the submodels that have more DOFs. The same trend continues in the post-buckling range where the 4-DOF submodels follow a lower, almost parallel path to the 2-DOF models, indicating that beyond the instability, as expected, interactive buckling dominates and the influence of overall bending diminishes.

Larger differences are observed in Fig. 10(b) for the case of a larger eccentricity, $e/b = 0.5$, where the load is effectively placed on the bottom face plate. This amplifies the difference between the early models and the 4-DOF submodels with the RBT 4-DOF model exhibiting a softer pre-buckling path and post-buckling response with a much lower limiting load than its 2-DOF equivalent. For the deeper beam ($b = 10.2$ mm), the merits of the RBT models in predicting the onset of localization earlier is clearly visible and more importantly the limiting loads predicted by the 4-DOF submodels are much lower than their 2-DOF counterparts as seen in Fig. 11.

5.2 *Sway versus tilt*

As before, the magnitude of tilt is plotted against the corresponding magnitude of sway. For the 4-DOF models, q_s is changed to $q_s + q_{sb}/4$ and that q_t is changed to $q_t + q_{tb}/\pi$, which refer to the maximum

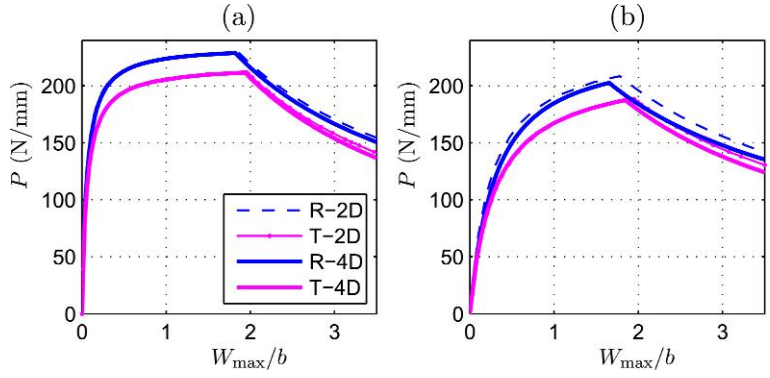

FIG. 10. Equilibrium paths of axial load versus overall panel displacement for different load eccentricities (a) $e/b = 0.1$ and (b) $e/b = 0.5$ for a sandwich panel 5.1 mm deep.

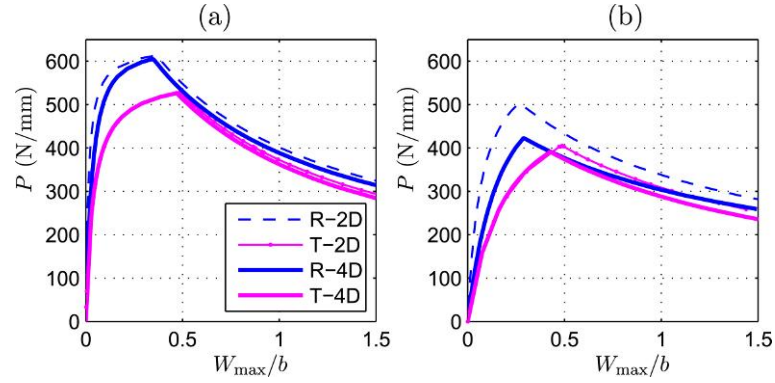

FIG. 11. Equilibrium paths of axial load versus overall panel displacement for different load eccentricities (a) $e/b = 0.1$ and (b) $e/b = 0.5$ for a sandwich panel 10.2 mm deep.

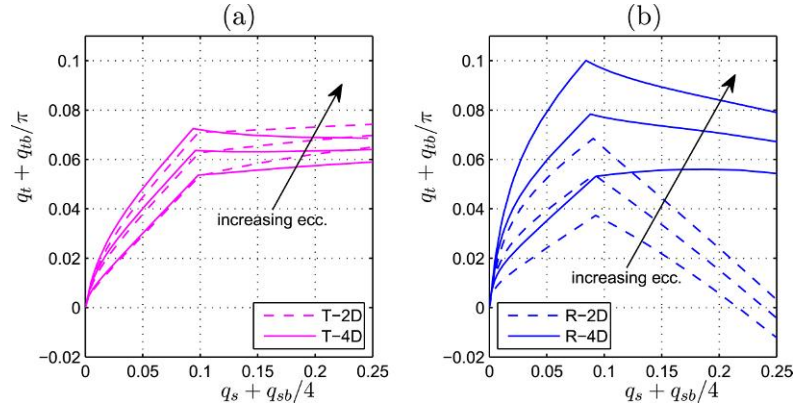

FIG. 12. Evolution of sway and tilt along the equilibrium path from small (lower paths) to large eccentricities for a 5.1 mm deep sandwich beam: (a) TBT models; (b) RBT models.

overall lateral displacement (over the length) and the maximum angle of tilt (over π), respectively (Fig. 12). The comparison of the TBT models against each other for different eccentricities shows that with increasing eccentricity, tilt increases faster for the 4-DOF models initially, while beyond the bifurcation point the tilt remains constant or even shows a minor decrease with increasing sway. This difference is even more pronounced when comparing the two RBT models where the amount of tilt initially increases much faster for the 4-DOF models, while beyond the point of instability the tilt shows at most only a small decrease as sway increases.

5.3 *Onset of interactive buckling*

At the bifurcation point, similar to the 2-DOF models as well as the pure strut case, interactive buckling is triggered because the local bending stress that is axially compressive on the bottom face plate exceeds its local buckling stress at midspan; this leads to localized buckling. However, since the current loading case has an eccentricity, the panel initially bends before any buckling occurs with a non-zero W and the local mode w is non-trivial comprising a small amplitude half sine wave shape that is derived from

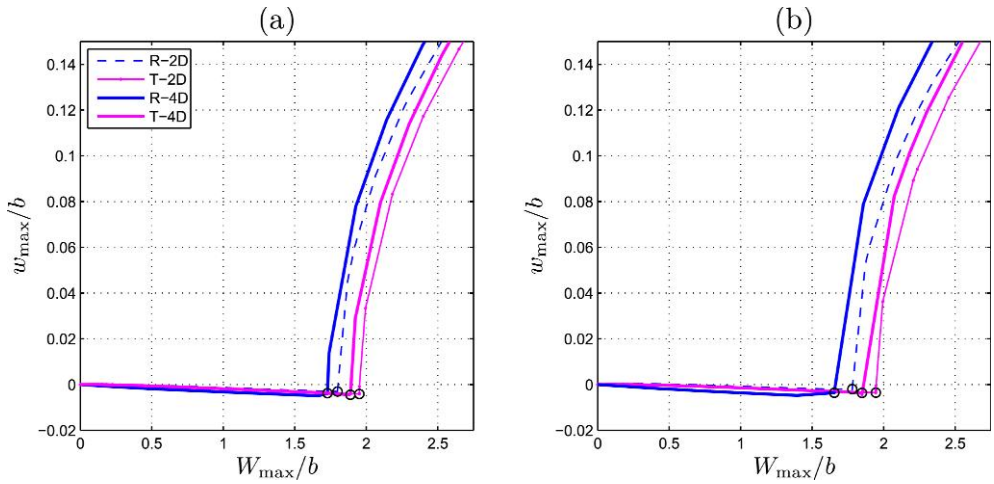

FIG. 13. The evolution of local and overall modes w and W, respectively, for a sandwich panel 5.1 mm deep. (a) $e/b = 0.3$, (b) $e/b = 0.5$. Limiting loads are denoted by $\circ$.

the forcing function, which appears in the final terms in (19) and (24) for the TBT and RBT models respectively. Beyond the bifurcation, the much shorter wavelength localized mode grows on top of the half sine wave almost independently in the sense that W and w are still linked through the equilibrium equations, albeit weakly. However, it is worth emphasizing that no localized wave perturbations are seen before the bifurcation point and that the pre-buckling path is akin to a non-trivial fundamental path, a topic that was covered in detail by Thompson & Hunt (1973). In Fig. 13, the evolution of the overall and local modes clearly shows that with increasing eccentricity the 4-DOF submodels predict an earlier onset of localization and a steeper development of the localized mode which leads to instability. In terms of the localized buckling profile, the results from the four models show similarities both in the number of peaks present, as well as the localized wavelength λ and wave height H as shown in Fig. 9.

5.4 *Validation*

The analytical formulations developed in this work are concerned with perfectly elastic sandwich panels with simple supports under the influence of an eccentric axial force. For validation purposes a fully numerical model was developed using the FE method within the commercial general purpose package ABAQUS (2006).

The sandwich panels were modelled with the geometric and material properties found in Section 3, following the steps outlined in Wadee *et al.* (2010). A 2D continuum was created with the plane stress assumption where only half the length of the panel was modelled by exploiting the inherent symmetry of the system. The core was modelled with the 2D solid element CPS4R, a four-noded bilinear element with reduced integration and hourglass control. Mesh convergence studies from the recent work (Wadee *et al.*, 2010) showed that 10 elements through the depth with an element aspect ratio close to unity sufficed to capture the structural response accurately. The face plates were modelled using stringers on the edges of the core. The use of stringers was deemed more favourable than 2D solid elements since it avoided shear locking in the face plate elements due to the large difference in the stiffness of the core and the face plates. Moreover, it was computationally less expensive since only one element was needed through the depth of the face plates. Lastly, by assuming stringers of specified geometric and material

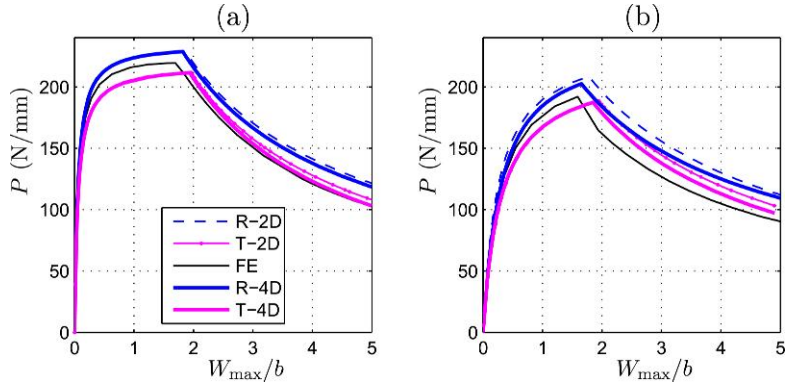

FIG. 14. Equilibrium paths for different load eccentricities (a) $e/b = 0.1$ and (b) $e/b = 0.5$ for a sandwich panel 5.1 mm deep.

properties bonded on the edges of the core, the modelling procedure resembled the analytical models closely. The stringers were discretized using B22 Timoshenko beam elements.

Simple support conditions were simulated by restraining the vertical displacement of the node at midheight of the loaded edge. The loaded edge was free to rotate and move horizontally, while at the other edge, the midheight node was restrained from rotation and horizontal displacement. The load was applied via load control with an adaptive step size. The loaded edge was constrained so that no localized stresses and deformations developed on the edge of the panel. Unlike the case of the strut problem, no overall imperfection was needed to initialize the solution (Belytschko *et al.*, 2000) since the eccentric loading acts as the necessary perturbation providing the initial bending necessary to trigger the instability. A number of simulations were devised and conducted for different eccentric loads to capture the lowest limiting load. The results are compared against the analytical models below.

5.4.1 *Equilibrium paths.* The equilibrium paths of the FE simulation are presented and compared with the equilibrium paths of the analytical models for different eccentricities (Fig. 14). The FE paths show a good correlation with a number of different aspects of the analytical models, especially when compared against the 4-DOF submodels. For the 5.1-mm-deep sandwich panel, the limiting loads predicted by the analytical models are very close to the ones predicted by FE; the 4-DOF submodels differing with the FE by up to 4%, and for the 2-DOF models up to 6% with the differences being greatest with increased e/b ratios. The improvement in the prediction of the limiting load is even more pronounced for the 4-DOF submodels in deeper beams that limit the maximum difference to 12% from 26% for the 2-DOF models. Further down the post-buckling path, these differences remain since the analytical post-buckling paths are almost parallel to the FE. Despite the differences observed in the load capacity, the 4-DOF submodels and FE have an excellent agreement in the rate of decrease of limiting loads with increasing eccentricity that seems to be approximately linear (Fig. 15). This is almost matched by both of the 4-DOF submodels even for the deeper sandwich panel that shows the greatest difference in the limiting loads.

One of the most favourable comparisons observed was for the initiation of interactive buckling and localization as expressed by the amount of lateral deflection and end shortening at the limiting load. The 4-DOF models exhibit a decrease in the limiting sway W^l required to trigger the interactive buckling mode with increasing eccentricity, unlike the 2-DOF TBT model where the limiting sway

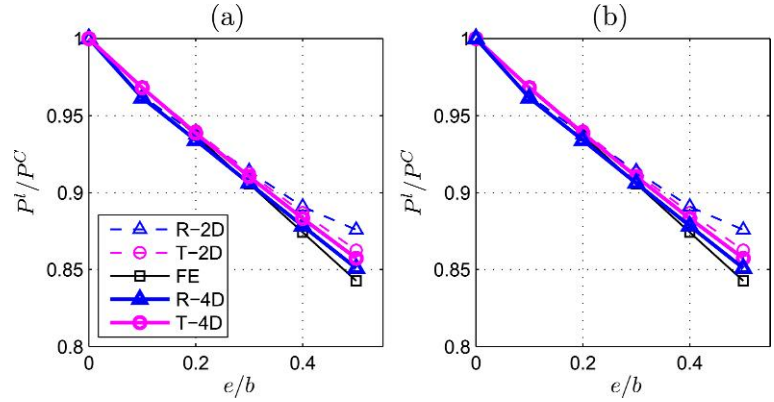

FIG. 15. Limiting loads P^l/P^{C} versus eccentricity values e/b for (a) a sandwich panel 5.1 mm deep and (b) a sandwich panel 10.2 mm deep.

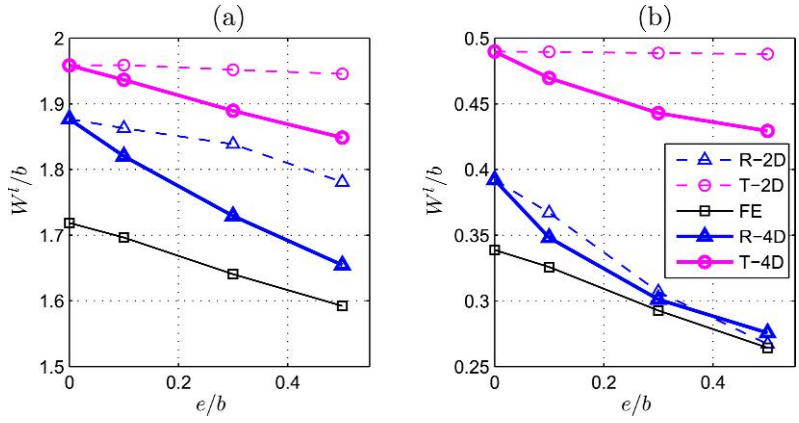

FIG. 16. Comparison of the limiting sway W^l for different eccentricities. (a) $b = 5.1$ mm, (b) $b = 10.2$ mm.

remains approximately the same regardless of the load eccentricity (Fig. 16). This is in strong agreement with the FE results. The inclusion of the extra DOFs increase the compressive stresses in the bottom face plate, thereby reducing the required sway before localized buckling; for larger eccentricities this effect is amplified.

5.4.2 *Localized buckling profiles.* The inclusion of the two extra DOFs improved the lateral displacement profile of the panel by introducing a small parabola in the overall bending in conjunction with the half sine wave for overall buckling. The FE-induced localized buckling shows an excellent qualitative correlation with all the analytical models. Quantitatively the two features that describe the localized mode is the wavelength λ and wave height of localization H (Fig. 9). Three different cases were examined, two for a sandwich panel 5.1 mm deep for different eccentricities ($e/b = 0.2, 0.5$) and one for a 10.2 mm panel and $e/b = 0.1$. The results are presented in Table 1 and are shown in Fig. 17(a–c).

TABLE 1 *The wavelengths of localization (λ) followed by the corresponding wave heights (H) in parentheses. All lengths are given in* mm. *The panels are all* 100 mm *long*

				TBT		RBT	
b	e/b	$\mathcal{E}/L$	FE	2D	4D	2D	4D
5.1	0.2	3.5%	14.2 (1.3)	12.9 (0.8)	12.1 (1.0)	12.6 (0.9)	12.7 (1.1)
5.1	0.5	4.0%	13.9 (1.7)	12.5 (1.0)	12.2 (1.2)	12.9 (1.2)	13.2 (1.4)
10.2	0.1	5.0%	15.2 (3.5)	16.2 (3.0)	14.9 (3.0)	17.5 (3.2)	16.5 (3.4)

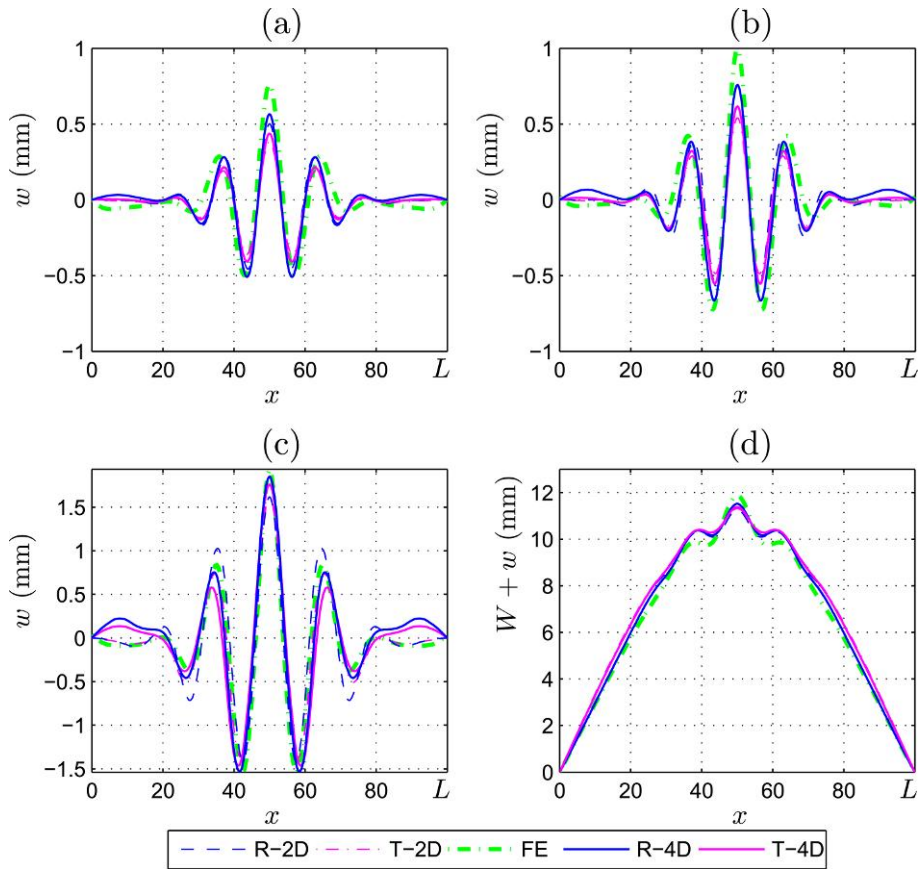

FIG. 17. (a)–(c) The local mode $w(x)$ profiles along the length. (a) 5.1 mm deep, $e/b = 0.2$ at $\mathcal{E}/L = 3.5\%$, (b) 5.08 mm deep, $e/b = 0.5$ at $\mathcal{E}/L = 4\%$, (c) 10.2 mm deep, $e/b = 0.1$ at $\mathcal{E}/L = 5\%$ and (d) the total deflection of the bottom face plate for the same parameters as in (a).

The wavelengths of the analytical models are within 2 mm of the FE result while, for the wave heights, the RBT 4-DOF effectively matches the ones obtained from FE. Fig. 17(d), which shows the total lateral displacement of the bottom face plate, including the overall displacement, clearly indicates the greater suitability of the 4-DOF models in comparison with the 2-DOF counterparts.

6. Summary and conclusions

Four increasingly sophisticated analytical models have been presented to account for interactive buckling in sandwich beam-columns. The applicability of the models is currently confined to sandwich panels where the axial load is offset from the panel neutral axis for bending, i.e. where the axial load and the moments are inextricably linked.

The first two models—one for TBT and one for the higher order RBT—only allowed for a half sine wave profile as the lateral displacement function which is the energetically favourable mode shape for overall buckling. Two further submodels were created—one for each bending theory—to incorporate the effects of overall bending due to the eccentricity in the application of the axial load. They were all formulated using energy principles and the governing nonlinear equations were solved in AUTO97. For validation purposes, an FE model was created using ABAQUS. The analytical models showed good correlation with the results from FE, with the 4-DOF submodels reducing the critical load and the corresponding level of sway with increasing load eccentricity. The RBT 4-DOF submodel compares very well with the FE results on the level of sway to initiate interactive buckling, as well as with the rate of decrease of the critical load with increasing eccentricity. Owing to its nonlinear in-plane core displacement, the same submodel also seems to be superior in estimating the onset of interactive buckling as the compressive stress threshold to cause localization is exceeded earlier. On the other hand, the TBT 4-DOF submodel is marginally better in estimating the maximum loads and the load carrying capacity in post-buckling, which suggests that a linear in-plane displacement may suffice to model the combination of bending and buckling in the post-buckling response of beam-columns. In any case, the analytical models have shown excellent agreement with the FE simulations for the localized buckling profiles and the 4-DOF submodels, in particular, seem to compare excellently for the total lateral displacement.

Further work on interactive buckling in sandwich panels is continuing with more general loading cases, such as those where moments are independent of the axial load. The approach in the current paper can be adapted in a relatively straightforward manner for more complicated loading scenarios. Moreover, the effect of using functionally graded core materials on the nonlinear buckling behaviour of sandwich panels is currently being investigated. These materials can be used effectively in conjunction with design optimization strategies since their properties can be tailored to the given design loading. It is therefore important to quantify their effect on the nonlinear buckling response; optimization schemes have been known to promote complex instabilities Thompson & Hunt (1973); Wadee (2000), but nonlinear modelling can inform designers of the regions in the parameter space where the interactive buckling is potentially less of an issue.

Acknowledgements

Stylianos Yiatros was supported by a UK Engineering and Physical Sciences Research Council Doctoral Training Award. The authors acknowledge the contribution of Marios Theofanous during the development of the FE models.

REFERENCES

ABAQUS. (2006) *Abaqus/Standard: User's Manual Version 6.6*. Pawtucket, RI: Hibbitt, Karlsson & Sorensen, Inc.

ALLEN, H. G. (1969) *Analysis and Design of Structural Sandwich Panels*. Oxford: Pergamon.

BANNINK, E., HADCOCK, R. & FORSCH, H. (1978) Advanced design composite material aircraft study. *J. Aircr.*, **15**, 661–669.

BELYTSCHKO, T., LIU, W. K. & MORAN, B. (2000) *Nonlinear Finite Elements for Continua and Structures*. Chichester: Wiley.

DOEDEL, E. J., CHAMPNEYS, A. R., FAIRGRIEVE, T. F., KUZNETSOV, Y. A., SANDSTEDE, B. & WANG, X-J. (1997) AUTO97: Continuation and bifurcation software for ordinary differential equations. *Technical Report.* Montreal, Canada: Department of Computer Science, Concordia University. Available at `ftp.cs.concordia.ca` in `/pub/doedel/auto`.

DRYSDALE, R. G., BETANCOURT-ANGEL, F. & HADDAD, G. B. (1979) Thick skin sandwich beam columns with weak cores. *ASCE J. Struct. Div.*, **105**, 2601–2619.

DUTHIE, A. C. (1987) Composite materials technology for helicopters. *Plastics Rubber Int.*, **12**, 20–24.

FAZIO, P., HUSSEIN, R. & HA, K. H. (1982) Sandwich beam-columns with interlayer slips. *ASCE J. Eng. Mech. Div.*, **108**, 354–366.

FOX, C. (1987) *An Introduction to the Calculus of Variations*. New York: Dover.

GIBSON, L. J. & ASHBY, M. F. (1999) *Cellular Solids: Structure and Properties*, 2nd edn. Cambridge Solid State Science Series. Cambridge: Cambridge University Press.

GLENDINNING, P. (1994) *Stability, Instability and Chaos: An Introduction to the Theory of Nonlinear Differential Equations*. Cambridge Texts in Applied Mathematics. Cambridge: Cambridge University Press.

HUNT, G. W. & WADEE, M. A. (1998) Localization and mode interaction in sandwich structures. *Proc. R. Soc. Lond. A*, **454**, 1197–1216.

HUNT, G. W., DA SILVA, L. S. & MANZOCCHI, G. M. E. (1988) Interactive buckling in sandwich structures. *Proc. R. Soc. Lond. A*, **417**, 155–177.

KNOX, E. M., COWLING, M. J. & WINKLE, I. E. (1998) Adhesively bonded steel corrugated core sandwich construction for marine applications. *Marine Struct.*, **11**, 185–204.

KODIYALAM, S., NAGENDRA, S. & DESTEFANO, J. (1996) Composite sandwich structure optimization with application to satellite components. *AIAA J.*, **34**, 614–621.

ØSTERGAARD, R. C. (2008) Buckling driven debonding in sandwich columns. *Int. J. Solids Struct.*, **45**, 1264–1282.

REDDY, J. N. (1984) A simple higher order theory for laminated composite plates. *Trans. ASME J. Appl. Mech.*, **51**, 745–752.

REDDY, J. N. (1990) A general non-linear third-order theory of plates of moderate thickness. *Int. J. Non-Linear Mech.*, **25**, 677–686.

SOKOLINSKY, V. & FROSTIG, Y. (1999) Nonlinear behavior of sandwich panels with a transversely flexible core. *AIAA J.*, **37**, 1474–1482.

THOMPSON, J. M. T. & HUNT, G. W. (1973) *A General Theory of Elastic Stability*. London: Wiley.

WADEE, M. A. (1999) Experimental evaluation of interactive buckle localization in compression sandwich panels. *J. Sandw. Struct. Mater.*, **1**, 230–254.

WADEE, M. A. (2000) Effects of periodic and localized imperfections on struts on nonlinear foundations and compression sandwich panels. *Int. J. Solids Struct.*, **37**, 1191–1209.

WADEE, M. A. (2002) Localized buckling in sandwich struts with pre-existing delaminations and geometrical imperfections. *J. Mech. Phys. Solids*, **50**, 1767–1787.

WADEE, M. A. & BLACKMORE, A. (2001) Delamination from localized instabilities in compression sandwich panels. *J. Mech. Phys. Solids*, **49**, 1281–1299.

WADEE, M. A. & HUNT, G. W. (1998) Interactively induced localized buckling in sandwich structures with core orthotropy. *Trans. ASME J. Appl. Mech.*, **65**, 523–528.

WADEE, M. A. & SIMÕES DA SILVA, L. A. P. (2005) Asymmetric secondary buckling in monosymmetric sandwich struts. *Trans. ASME J. Appl. Mech.*, **72**, 683–690.

WADEE, M. A., YIATROS, S. & THEOFANOUS, M. (2010) Comparative studies of localized buckling in sandwich struts with different core bending models. *Int. J. Non-Linear Mech.*, **45**, 111–120.